JOURNAL OF MATERIALS SCIENCE 17 (1982) 2077–2086

Defects on $TlBiTe_2$ single crystals

E. K. POLYCHRONIADIS, J.STOEMENOS
Department of Physics, University of Thessaloniki, Thessaloniki, Greece

Single crystals of rhombohedral $TlBiTe_2$ examined by transmission electron microscopy consist of large areas separated by {100}- and {110}-type twins. By measuring the rhombohedral angle from the splitting of diffraction patterns in the twin areas, we calculated the residual strain which remained after the transformation $O_h \rightarrow D_{3d}$, ranging from 1.2 to 12.2%. Dislocations with Burgers vector $(a/2)\langle 1\bar{1}0\rangle$ were mobile and the main slip system was $(111)\langle 1\bar{1}0\rangle$. Planar defects with complex α–δ fringe contrast were also observed.

1. Introduction

The compound $TlBiTe_2$ has recently appeared as an interesting compound for acousto-optic applications [1]. It also has a high thermoelectric figure of merit, so it presents interesting electrical properties [2, 3]. There is also considerable structural interest, since $TlBiTe_2$ may be regarded as "pseudo-PbTe" [4–8].

At room temperature the structure of $TlBiTe_2$ can be described as NaCl-type, which has a slight rhombohedral distortion with an elongation along the [111] axis, while an ordering of successive layers occurs normal to the rhombohedral axis in the sequence –Tl–Te–Bi–Te [9] (Fig. 1). The space group is $R\bar{3}m$-D^5_{3d}, the lattice parameter of the primitive cell is $a_0 = 0.8137$ nm and the rhombohedral angle, $\alpha = 32°18'$.

Recently the authors succeeded in growing single crystals of an adequate size [10]. On the basis of the above considerations the aim of the present work was to study the defect structure of $TlBiTe_2$ single crystals by transmission electron microscopy (TEM).

2. Experimental procedure

The $TlBiTe_2$ crystals were prepared from commercially available 99.999% pure elements and single crystals of an adequate size were grown using a modified Bridgman technique. The specimens were prepared by a combination of chemical electropolishing and ion bombardment [10]. For the observations, a JEM 120 CX electron microscope operating at 100 kV was used.

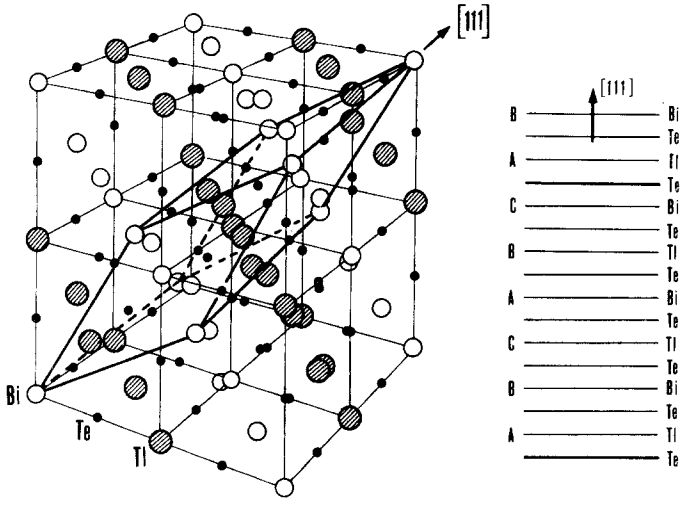

Figure 1 (a) Structure of rhombohedral $TlBiTe_2$. The thicker lines represent the primitive unit cell. (b) Successive layers of atoms perpendicular to the rhombohedral axis in the sequence Tl–Te–Bi–Te.

0022–2461/82/072077–10$03.70/0

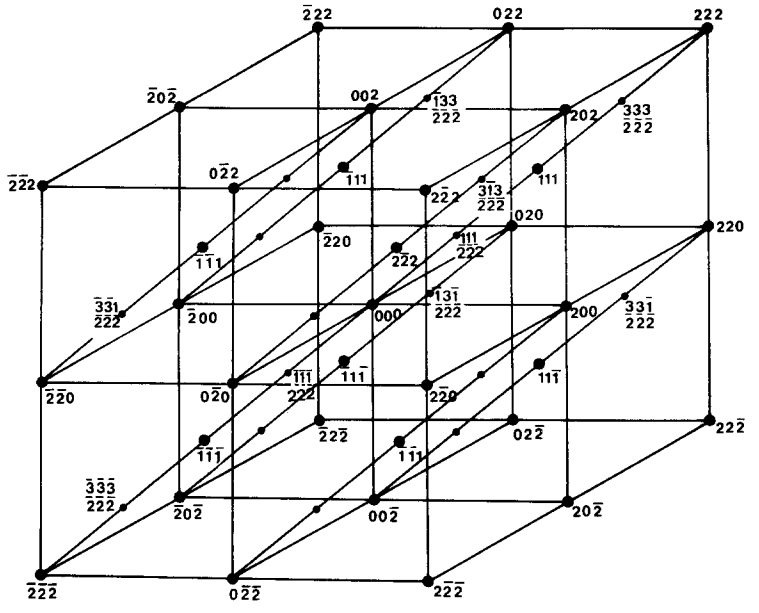

Figure 2 Reciprocal lattice of ordered $TlBiTe_2$. The small dots denote super-lattice reflections.

3. Observations and results

3.1. Twins

The $TlBiTe_2$ structure, already been mentioned, can also be described as a non-primitive rhombohedral cell which is slightly different from a cubic cell. This multiple cell has 16 Tl, 16 Bi and 32 Te atoms, a lattice parameter of $a_0 = 1.2988$ nm and a rhombohedral angle, $\alpha = 88°21'$. This unit cell is compatible with the superlattice spots of $(\frac{1}{2}\frac{1}{2}\frac{1}{2})$ that appear along the [111] direction and verify the ordering of Tl–Te–Be–Te layers normal to the three-fold axis. Tilting experiments allowed the construction of the reciprocal lattice as shown in Fig. 2 where the small dots denote superlattice reflections that agree with the calculation of the structure factors done previously [9].

Electrical measurements [3], as well as a differential thermal analysis (DTA) study, verify a phase tranformation of $O_h \rightarrow D_{3d}$ which occurs at 426° C. Using this fact, a group theory treat-

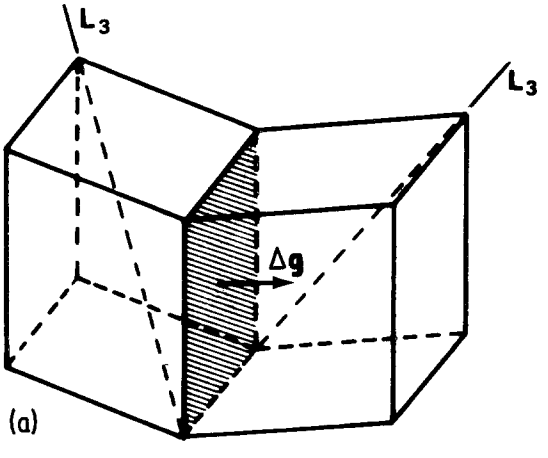

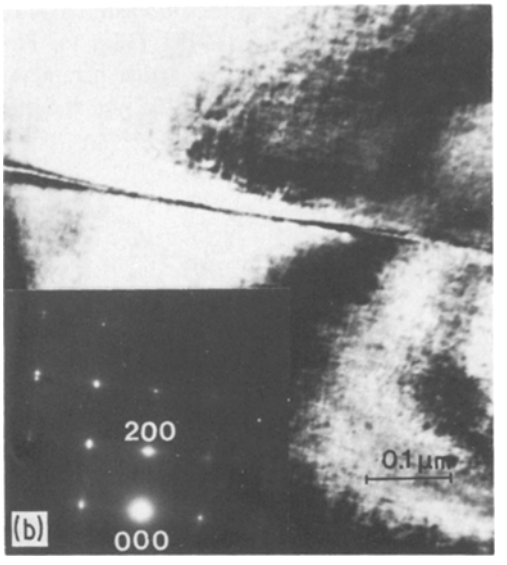

Figure 3 (a) Three-dimensional diagram of a (100)-type twin and the related twin vector $\Delta\mathbf{g}$ in the reciprocal space. (b) Coherent (100) twin boundary and related diffraction patterns from the twin boundary. The row of spots along [100] is unsplit. Residual strain exists along the composition plane as can be verified by noting the displacements of the fringes crossing the boundary.

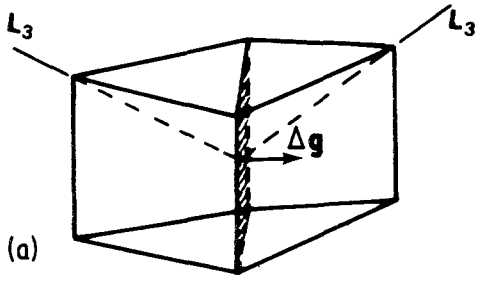

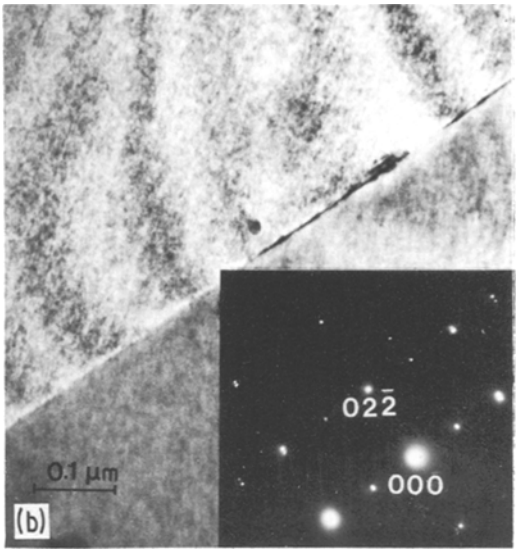

Figure 4 (a) Twin of the (1 1 0) type and the related twin vector Δg in the reciprocal space. (b) Coherent (0 1 1) type twin with the twin boundary parellel to the electron beam. The unsplit row of spots along the [0 1 1] direction.

ment has already been applied to find the types of transformation twins that were to be expected in $TlBiTe_2$ at room temperature [9]. These were coherent {1 0 0} and {1 1 0} twins and semicoherent {1 0 0} twins.

The general geometrical analysis methods for calculating the twin vectors, Δg, for lattices with small deviations from structures with higher symmetry have been described by Gevers *et al.* [11, 12]. The vector Δg which defines the separation between corresponding reciprocal lattice vectors g_1 and g_2 in the matrix and in the twin, respectively, is always parallel to the twin axis. If there is a [1 1 1] rhombohedral axis, then, for coherent twins of (1 0 0)-type, the magnitude $|\Delta g|$ is given by $|\Delta g| = 2\theta(k + l)/a_0$, where $h\,k\,l$ are the Miller indices and a_0 the lattice constant for the slightly distorted non-primitive cubic cell, $\theta = 90\text{-}\alpha = 1°39'$. If the (1 0 0) twin boundary is parallel to the electron beam, then the splitting of the spots is $|\Delta g| = 2\theta k/a_0$. The splitted $\{0k0\}$ spots are parallel to the unsplitted row of $\{h00\}$ spots (Fig. 3).

For {1 1 0}-type twins, vector Δg is again

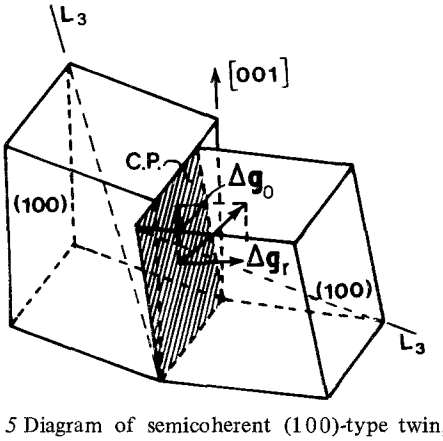

Figure 5 Diagram of semicoherent (1 0 0)-type twin, the related twin vector Δg and its components Δg_0 along [0 0 1] and Δg_r along [1 0 0].

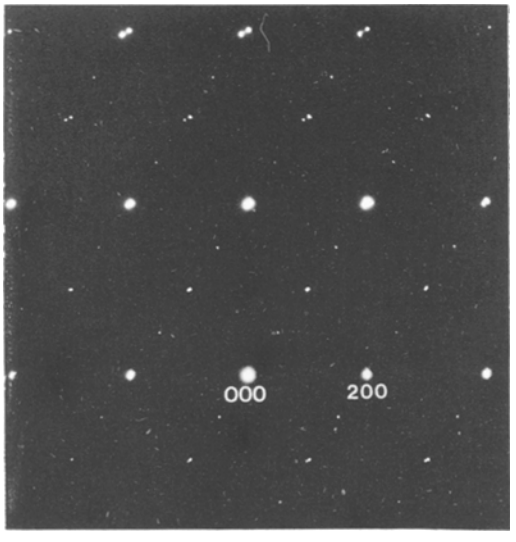

Figure 6 Diffraction patterns from a semicoherent (1 0 0)-type twin in a (0 1 1) section. Unsplit row of spots along the [1 0 0] direction. The splitting of the spots is not parallel to the unsplit row. Superlattice spots are not split.

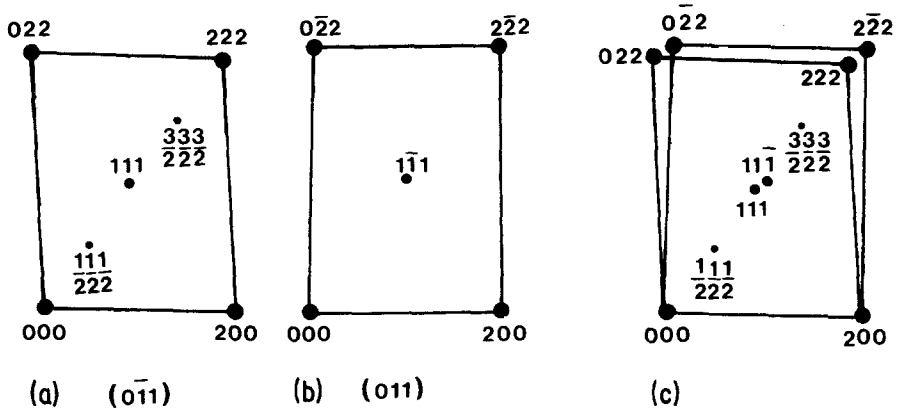

Figure 7 (a) Diffraction patterns from a single domain at area A of Fig. 8. Foil section (011). (b) Diffraction patterns from a single domain at area B adjacent to A. (c) Diffraction patterns from areas A and B.

perpendicular to the twin plane and for twin boundaries, inclined at 45° as to the electron beam, the component perpendicular to the electron beam has a magnitude $|\Delta \mathbf{g}_r| = 2\theta(k/a_0)$, while for {110} twin boundaries, parallel to the electron beam, the magnitude was $|\Delta \mathbf{g}| = 2^{\frac{1}{2}}|\Delta \mathbf{g}_r|$ (Fig. 4).

In semicoherent (100) twins the composition plane (CP) is the (100) one. Vector $\Delta \mathbf{g}$ could be analysed in two components, with the same magnitude equal to $2\theta(k/a_0)$ with one $\Delta \mathbf{g}_0$ parallel to the [001] axis and the other $\Delta \mathbf{g}_r$ parallel to the [100] axis (Fig. 5). For a (001) foil, it is impossible to distinguish by the diffraction patterns the semicoherent (100) twins from the coherent ones of the same type since the splitting of $hk0$ reflections is the same. This is because the $\Delta \mathbf{g}_0$ component for semicoherent twins is invisible, the two spots being superimposed. Nevertheless semicoherent twins of the (100)-type give characteristic diffraction patterns for a foil section

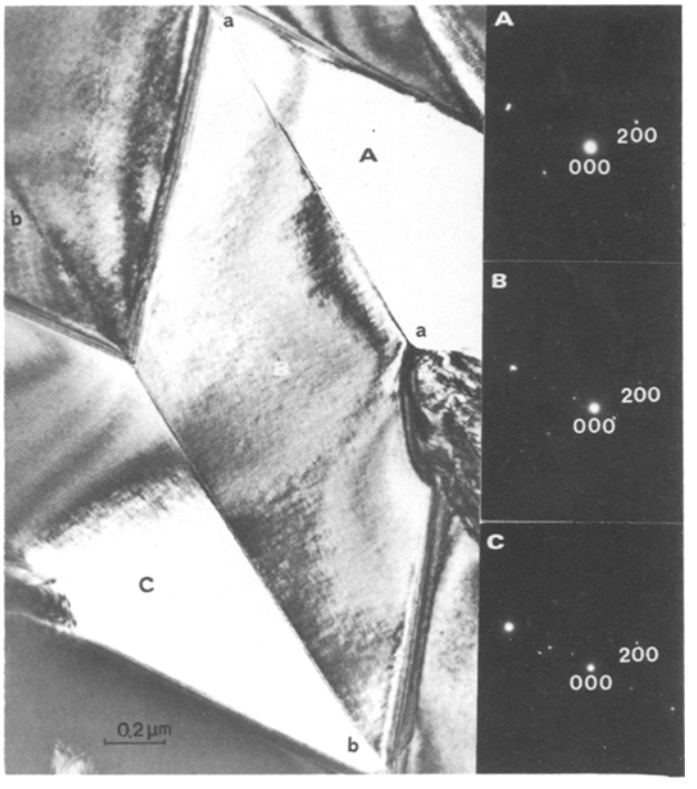

Figure 8 Semicoherent (100)-type twins at aa and bb. Foil section (011).

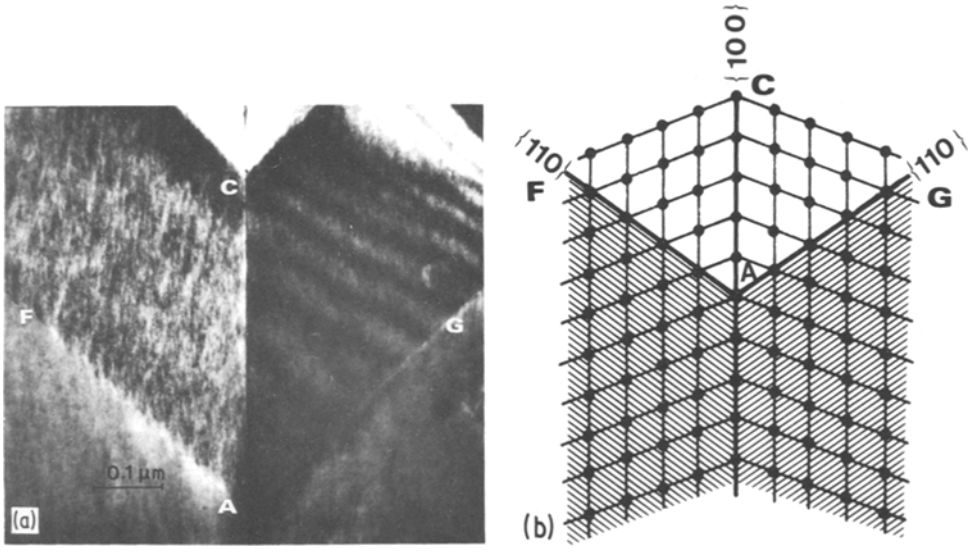

Figure 9 (a) Twins of the (100)-type at A and C internally broken by (110) twins at F and A as well as A, G. Foil section (001). (b) Projection of the same arrangment in the (100) section.

(110), where the splitting of the spots is not parallel to the unsplit row of diffraction patterns, Fig. 6, obtained from the adjacent crystals in the twin boundary.

From Fig. 5 it is clear that the three-fold axis in the two parts of the twin skew and the superlattice spots do not appear simultaneously in the diffraction pattern. We can now construct reciprocal lattice planes that could explain the electron diffraction patterns of Fig. 6. Constructing the $(0\bar{1}1)$ reciprocal lattice plane for the matrix, Fig. 7a, and the (011) plane for the twin, Fig. 7b, we can superimpose them as in Fig. 7c. Since the (100) planes are parallel to the composition plane, $h00$ spots form an unsplit row. The lattice modes $(\bar{2}\bar{2}\bar{2})$ and $(\bar{2}2\bar{2})$ as well as the $(0\bar{2}\bar{2})$ and (022) are not in the same plane. Moreover, they come close to Ewald's sphere simultaneously so that diffraction patterns of Fig. 6 correspond to Fig. 7c. Semicoherent {100}-type twins have been identified in a (110) foil section, Fig. 8, where aa and bb are the composition planes.

The arrangement of the twins in the well-developed single crystals consists mainly of bands of coherent {100} twins of about 1 μm width broken internally by {110} twins (Fig. 9). In this way, it is possible for the three different twin boundaries to meet and remain coherent.

Measuring the splitting $|\Delta\mathbf{g}|$ from the diffraction patterns for the several types of twins it was possible to calculate precisely the angle which gives the deviation from cubic symmetry. Formally this angle should be $90° - \alpha = 1.65°$, but it was always found to be less than this, having values between 1.63° and 1.45°. This indicates that twinned areas are under a strain ranging from 1.2 to 12.2%. Probably this is one reason why the twin boundaries act as sources of dislocations as we shall see in the next section.

3.2. Dislocations

Dislocations frequently appeared in large twin areas. Most of them were extremely mobile, leaving strong slip traces along the $\langle 1\bar{1}0\rangle$ directions. Fig. 10a, b, c is a sequence taken in 30 sec intervals. The dislocations bowed out and then moved in a jerky manner in the thicker part of the crystal, as can be deduced from the slip traces becoming progressively wider. The contrast of the traces persisted over a long period of about three months. Although in Fig. 10 the movement of the dislocations was due to the electron beam, as a result of the thermal stress, this was not always the case. Dislocations in general were stable under the electron beam but very often they moved spontaneously as we can deduce from systematic observation of the same area (Fig. 11) for time intervals of two weeks. In order to avoid producing stress we kept the specimen in the same holder all the time. It is clear that many dislocations moved, as can be deduced from the traces they have left behind (Fig. 11a, b, c). The movement of the dislocations is probably due to the internal stress to which the twinned areas are

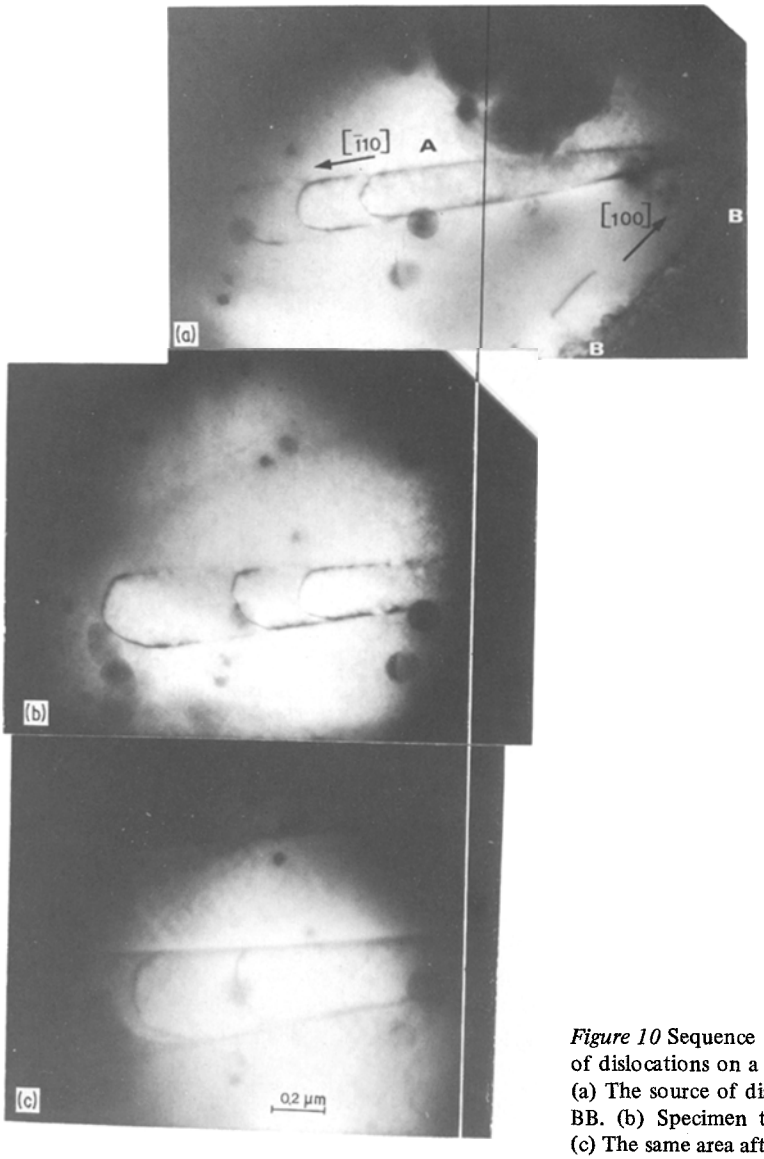

Figure 10 Sequence of photographs showing movement of dislocations on a (1 1 1) slip plane. Foil section (0 0 1). (a) The source of dislocation is the (0 1 0) twin boundary BB. (b) Specimen tilted along the [$\bar{1}$ 1 0] axis for 15°. (c) The same area after 30 sec.

subjected, directly connected with the distortions in the lattice, as already mentioned in the measurements of the splitting of the spots in Section 3.1.

Tilting experiments show that only one slip plane exists, the plane (1 1 1) perpendicular to the rhombohedral axis. When this plane is parallel to the electron beam, it gives super-lattice reflections of the type $(\frac{1}{2}\frac{1}{2}\frac{1}{2})$. Primary slip planes in rock-salt-type crystals are $\{1\,1\,0\}$ or $\{1\,0\,0\}$, so our observation was unexpected, if we consider than in the case of $TlBiTe_2$ there is only a slight deviation from the NaCl-type structure. Nevertheless the calculations of the distances in the unit cell taking into account the ordering of –Tl–Te–Bi–Te– (Fig. 1) show that the type of the atomic bonds is partly covalent and partly ionic, a fact which weakens the electrostatic binding. The good cleavage of the $TlBiTe_2$ single crystals perpendicular to the rhombohedral axis is also proof of the weak atomic binding along the (1 1 1) plane.

All the mobile dislocations have $(a/2)\langle 1\,\bar{1}\,0\rangle$ Burgers vector as the tilting experiments reveal. This is the shortest possible perfect dislocation Burgers vector for the NaCl-type crystals. Very often the dislocation can cross the twin boundaries. In order to cross the twin boundary, a dislocation should have a Burgers vector in common with the slip planes on either side of it. In our case, the slip plane is (1 1 1) and the dislocation that glides has a Burgers vector $(a/2)\langle 1\,\bar{1}\,0\rangle$ so twin boundaries

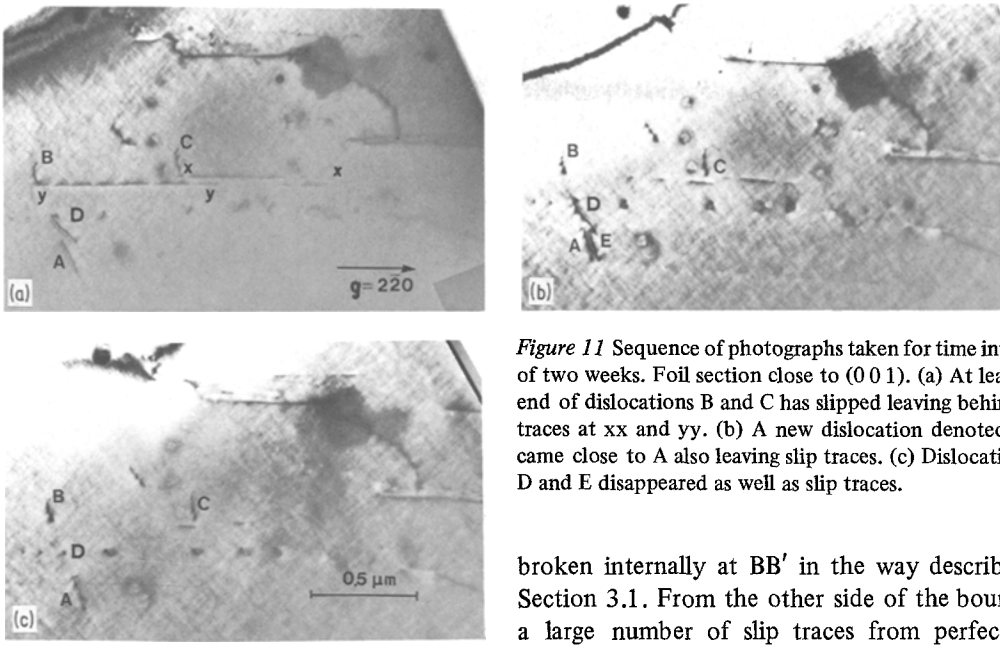

Figure 11 Sequence of photographs taken for time intervals of two weeks. Foil section close to (0 0 1). (a) At least one end of dislocations B and C has slipped leaving behind slip traces at xx and yy. (b) A new dislocation denoted by E came close to A also leaving slip traces. (c) Dislocations at D and E disappeared as well as slip traces.

of the {100}- and the {110}-type satisfy these conditions.

Twin boundaries are the main dislocation sources as can be seen in Fig. 12, where the twin boundary of the (100)-type, labelled AA′, is perpendicular to the foil. One side of the twin is broken internally at BB′ in the way described in Section 3.1. From the other side of the boundary a large number of slip traces from perfect dislocations emitted from the boundary are evident. The lower part of the twin at A is bent leading to a lenticular shape. The boundary is no longer coherent so that twinning dislocations must have been created on the boundary although they are invisible since the boundary is parallel to the electron beam. Now the density of the emitted

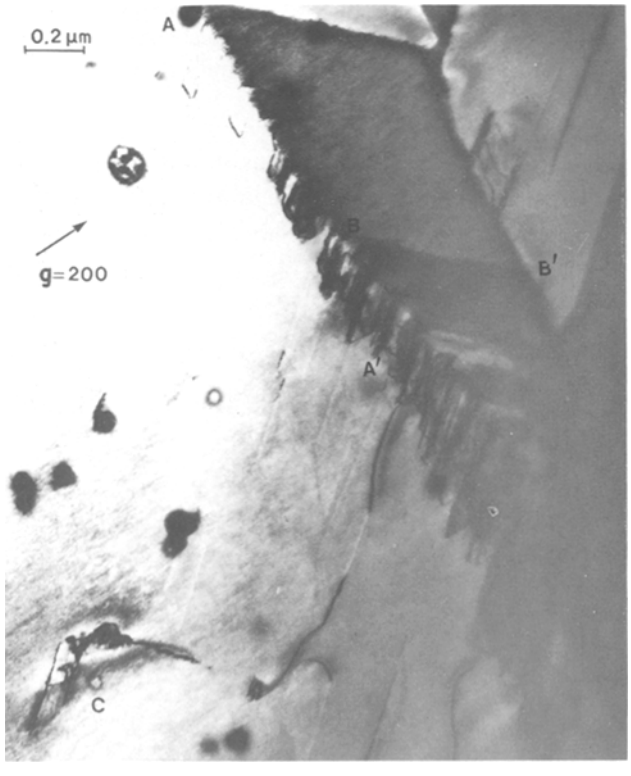

Figure 12 Dislocation movement from a twin boundary of (100) at AA′. Notice that the boundary is slightly curved in the lower part of the photograph. The twin boundary is broken inside by {110}-type twins BB′. A planar fault is denoted at C. Foil section (001).

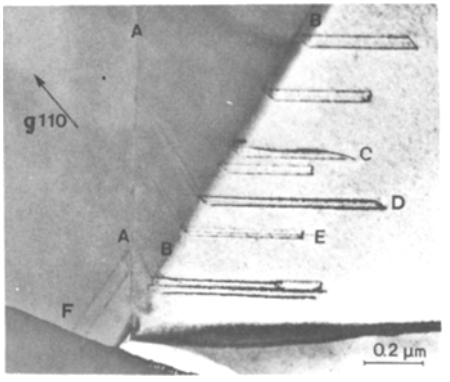

Figure 13 Twin boundary (0 1 $\bar{1}$), denoted by AA while the (0 1 0) plane is denoted by BB. Foil section ($\bar{1}$ 1 1).

dislocations increases rapidly, so that the slip traces superimpose, revealing a very high stress.

The relationship between twinning dislocations and emitted dislocations from a twin boundary can be seen in Fig. 13, where a combination of (1 1 0)-type twins, labelled AA, and (1 0 0)-type twins, labelled BB, are present. The foil section is now ($\bar{1}$ 1 1) so that the (0 1 $\bar{1}$) twin boundary is parallel to the electron beam while the (0 1 0) twin boundary is inclined to it. Clearly, the sources of the dislocations emitted from boundary B are related with dislocations lying in the boundary. The dislocation at C shows only one slip trace since the other side is pinched off at the boundary. Slip bands at D and E are extended from both sides of the boundary although dislocations are visible only on the right side. It is possible for a dislocation from the left side to move and penetrate the boundary if the Burgers vector of the slip dislocation is parallel to the line of intersection of the twin and the slip planes. Moreover, dislocations that cross a (1 0 0) twin cannot cross a twin of (1 1 0)-type also since the same Burgers vector does not satisfy the common condition simultaneously. Slip traces are evident at F near the (0 1 $\bar{1}$) twin showing larger band widths compared with those at C, D and E, since the projection of the slip planes on the plane of the foil is different.

Dislocations could also slip along the twin boundary as can be seen in Fig. 14a, where the boundary AB is a (0 1 1) twin and the foil section is (0 0 1).

From the slip traces it is evident that a dislocation at C, near the edge of the specimen, glided on the (1 1 1) plane and met the boundary at D. There the slip traces changed direction and the glide took place along the twin boundary and finally stopped at E, where a dislocation is visible. Since the Burgers vector of the dislocations gliding on the (1 1 1) plane were of the $(a/2)\langle 1\bar{1}0\rangle$ type, the dislocation could cross-slip at D only if its Burgers vector was $(a/2)[0\bar{1}1]$, a vector common also the to (0 1 1) plane. Nevertheless, the dislocations at E becomes invisible for $\mathbf{g} = \bar{2}20$ (Fig. 14b) excluding a Burgers vector of $(a/2)[0\bar{1}1]$. It is obvious that an interaction of the glide dislocation and the twin boundary took place. In Fig. 14a the operated reflection was the common (0 2 0) one, so that no δ-fringe contrast appeared, although some residual contrast existed, revealing the strain in the composition plane.

3.3. Planar defects

Fringe patterns were often observed while partial dislocations were always present along the borders

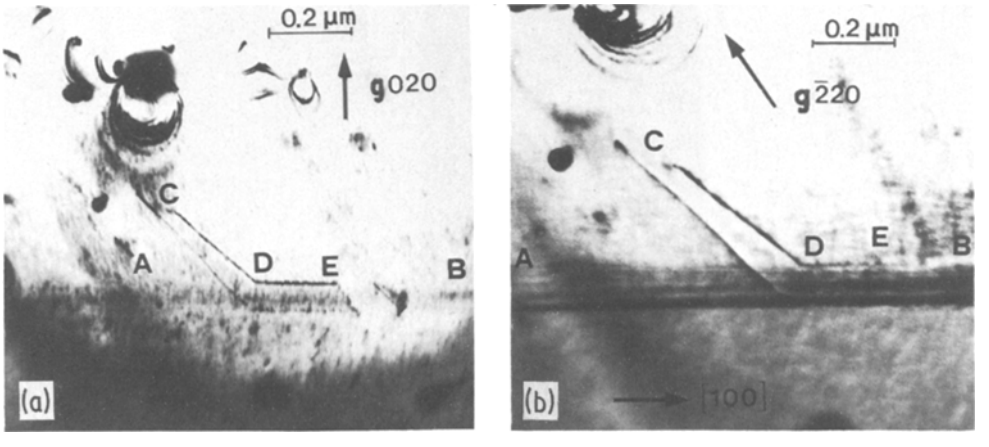

Figure 14 Twin boundary of (0 1 1) at AB. Foil section (0 0 1). (a) Operating reflection g(0 $\bar{2}$ 0). (b) Operating reflection g($\bar{2}$ 2 0).

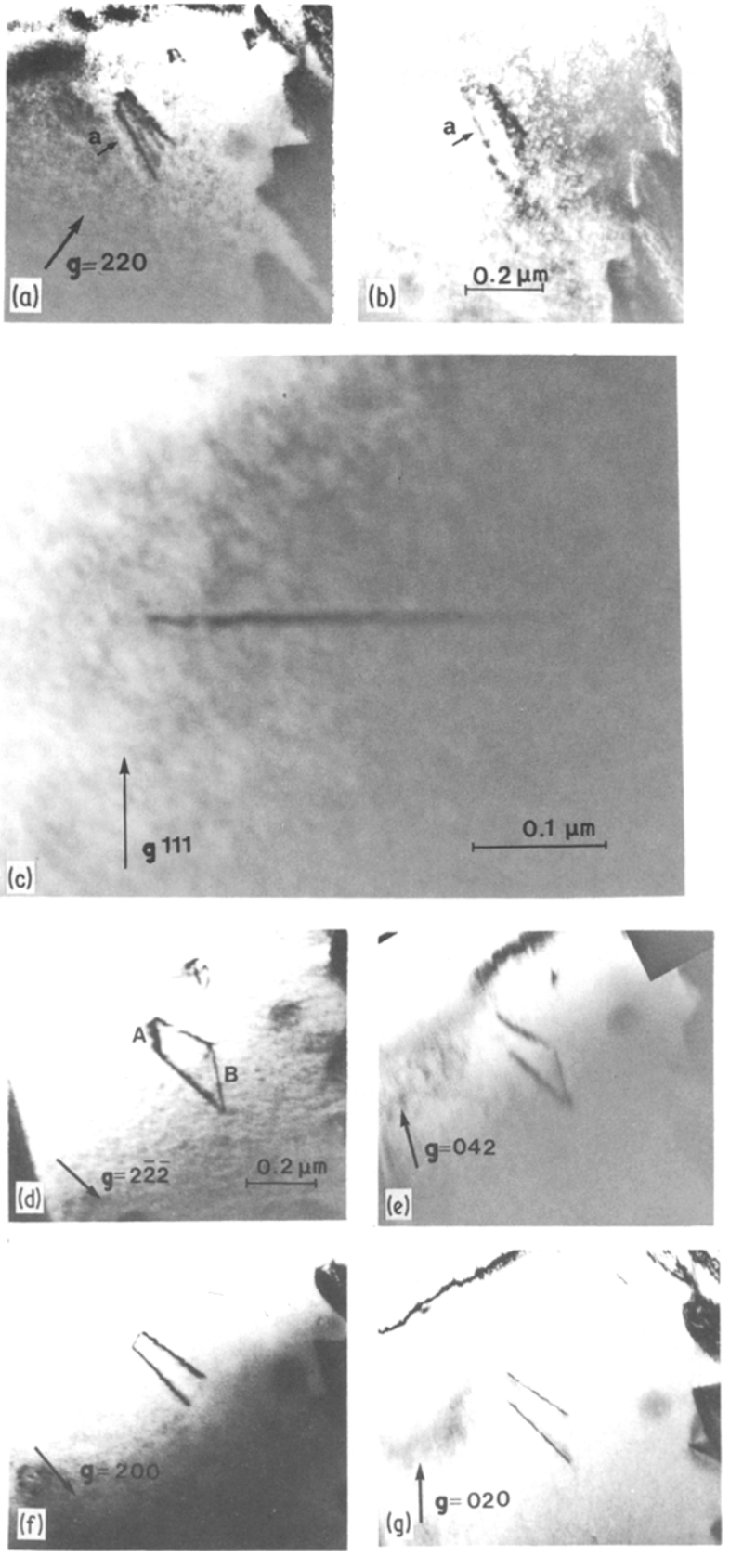

Figure 15 Foil section (001). (a) Bright-field. The fringes are $\alpha-\delta$ type since there is a faint constrast from the outer fringe denoted by arrow a. (b) Dark-field. (c) Specimen tilted, plane of the fault parallel to the electron beam. (d) Both dislocations at A and B are visible. (e) Dislocation at A is invisible. (f) Dislocation at B is out of contrast. (g) Both dislocations are invisible.

TABLE I Burgers vector determination of partial dislocations. The image of the dislocation will be effectively invisible if [14] $\mathbf{g} \cdot \boldsymbol{b} = 1/3$ and $m = 1/8(\mathbf{g} \cdot \boldsymbol{b} \wedge \mathbf{u}) \leqslant 0.08$

g	$\boldsymbol{b}$	
	$\frac{1}{6}[\bar{2}11]$	$\frac{1}{6}[11\bar{2}]$
020	$\mathbf{g} \cdot \boldsymbol{b} = \frac{1}{3}, m = 0.06$	$\mathbf{g} \cdot \boldsymbol{b} = \frac{1}{3}, m = 0.03$
200	$\mathbf{g} \cdot \boldsymbol{b} = \frac{2}{3}, m = 0.06$	$\mathbf{g} \cdot \boldsymbol{b} = \frac{1}{3}, m = 0.03$
$04\bar{2}$	$\mathbf{g} \cdot \boldsymbol{b} = \frac{1}{3}, m = 0.06$	$\mathbf{g} \cdot \boldsymbol{b} = 1, m = 0.03$
$2\bar{2}\bar{2}$	$\mathbf{g} \cdot \boldsymbol{b} = -\frac{4}{3}, m = 0.06$	$\mathbf{g} \cdot \boldsymbol{b} = \frac{2}{3}, m = 0.03$

of the fringes; the tilting experiment showed that the fault plane coincided with the main slip plane (111). These faults could not be attributed to a typical stacking fault, since the outer parts of the fringes were different from those of the inner part, as seen from the bright- and dark-fields in Fig. 15a, b (see also Fig. 12 at C). The contrast could be attributed to mixed α–δ boundaries, as in the case reported by Van Landuyt *et al.* [13] in niobium where they were caused by thin precipitates. The fault was interpreted by a central region overlapped by two closely spaced interfaces, the constrast arising from a slight misorientation of the reflecting planes of the matrix and the precipitate. For this reason, we tilted the specimen so that the plane of the fault was parallel to the electron beam (Fig. 15c). We found a mean thickness of 5.0 nm, that means the fault is extended to about 25 atomic layers along the [111] axis. A possible explanation for the appearance of the precipitations is a deviation from the stoichiometry. Indeed, chemical analysis revealed a stoichiometric composition of $Tl_{0.93}Bi_{1.07}Te_2$. The Burgers vectors of the partial dislocations were identified (Table I) to be those of the $\frac{1}{6}a$ [11$\bar{2}$]-type (Fig. 15).

4. Conclusions

All the twin types predicted theoretically were observed, although a residual strain remained near the twin boundaries and was mainly the source of dislocation emitted by the boundaries. In Fig. 10a the source of the dislocations is the (010) twin boundary, the slip plane is (111) and the foil section close to (001). If it is assumed that a Frank–Read source operates there, we can estimate the stress required to cause the dislocations. Thus the slip traces near the twin boundary show that the pinning points are at a distance $l = 0.22\,\mu$m while the Burgers vector $b = (a/2)\langle 1\bar{1}0\rangle$ has a magntiude 0.46 nm so that to a first approximation the stress is $r \simeq (\mu b)/l \simeq \mu/470$.

Perfect dislocations from the matrix can interact with the twin boundaries to form twin boundary dislocatons (Fig. 15). From this point of view the glide of a dislocation along [100] on a (011) plane should be closely related to twin boundaries and not considered to be a second slip system. Stereophotographs revealed that not all the dislocations were laid on the (111) plane.

Very often transformation twins meet each other along non-coherent interfaces that were low-angle boundaries, accompanied by a set of dislocations distributed uniformly along them.

In conclusion the findings presented here verify the sudden jump in the number of carriers at the tranformation temperature as deduced from the electrical measurements [3], since above this temperature the high density of the twin boundaries that act as localized states disappeared.

References

1. R. S. FEIGELSON, *Jap. J. Appl. Phys.* 19 (1980) Suppl. 19–3, 371.
2. R. A. HEIN and E. M. SWIGGARD, *Phys. Rev. Lett.* 24 (1970) 53.
3. O. VALASSIADES, E. K. POLYCHRONIADIS, J. STOEMENOS and N. A. ECONOMOU, *Phys. Stat. Sol. (a)* 65 (1981) 215.
4. S. A. SEMILETOV and L. I. MAN, *Sov. Phys. Crystallogr.* 4 (1960) 385.
5. E. F. HOCKINGS and J. G. WHITE, *Acta Cryst.* 14 (1961) 328.
6. L. I. MAN and S. A. SEMILETOV, *Sov. Phys. Crystallogr.* 7 (1963) 686.
7. B. T. KOLOMIETS and N. A. GORYUNOVA, *Zh. Tekhn. Fiz.* 25 (1955) 984.
8. S. A. DEMBOVSKII, *Trans. Inorg. Mater.* 4 (1968) 1671.
9. E. K. POLYCHRONIADIS, G. L. BLERIS and J. STOEMENOS, *Thin Solid Films* 37 (1976) 407.
10. E. K. POLYCHRONIADIS, J. STOEMENOS, *Cryst. Growth* 55 (1981) 388.
11. R. GEVERS, P. DELAVIGNETTE, H. BLANK and S. AMELINCKX, *Phys. Stat. Sol.* 4 (1964) 383.
12. R. GEVERS, P. DELAVIGNETTE, J. VAN LANDUYT and S. AMELINCKX, *Phys. Stat. Sol.* 5 (1964) 959.
13. J. VAN LANDUYT, R. GEVERS and S. AMELINCKX, *Phys. Stat. Sol.* 13 (1966) 467.
14. I. HOWIE and M. J. WHELAN, *Proc. Roy. Soc. A* 267 (1962) 206.

Received 17 November
and accepted 14 December 1981